The International Journal of Advanced Manufacturing Technology
https://doi.org/10.1007/s00170-025-17198-9

ORIGINAL ARTICLE

Investigation of the formation and reduction of hydrogen porosity during laser welding of additively manufactured AlSi10Mg parts

Steffen Kramer[1,2] · Victor Lubkowitz[2] · Michael Haas[1] · Johannes Michel[1] · Christoph Spurk[3] · Alexander Olowinsky[4] · Guilherme Abreu Faria[5] · Michael Jarwitz[1] · Thomas Graf[1] · Volker Schulze[2] · Frederik Zanger[2]

Received: 21 September 2025 / Accepted: 5 December 2025

Abstract
With the increasing industrial implementation of additively manufactured metal parts, the welding of such components gains importance. Due to size limitations of laser powder-bed fusion (PBF-LB) machines and design constraints, subsequent joining processes are required. However, the weld seam quality of PBF-LB manufactured parts, particularly aluminum parts, is still limited by pore formation in the weld seam. These pores are believed to be primarily caused by the agglomeration of hydrogen. Therefore, this study investigates the pore formation during laser beam welding of PBF-LB manufactured AlSi10Mg parts by means of in-situ high-speed synchrotron X-ray imaging. In addition, an in-situ laser powder drying process is investigated to reduce the hydrogen content of PBF-LB manufactured aluminum parts in order to prevent the formation of hydrogen porosity during the subsequent welding process. Results show that pores predominantly form in the interdendritic region at the solidification front due to the locally increased hydrogen concentration. By applying laser powder drying, the hydrogen content can be reduced by up to 25%, thereby effectively preventing the formation of hydrogen pores.

Keywords Laser welding · Powder bed fusion (PBF-LB) · AlSi10Mg · Hydrogen pores · Weld seam quality · High-speed x-ray imaging

1 Introduction

Additively manufactured parts experience an increased implementation in industrial applications. In the aviation and aerospace sector, for example, aluminum cast parts are substituted with parts manufactured with laser powder bed fusion (PBF-LB) due to their benefit in weight and strength [1]. The size limitations for PBF-LB parts set by the process chamber and the integration of these parts into larger assemblies, however, necessitate a consecutive joining process [2, 3]. This is mostly done by laser beam welding, as this process allows high productivity and flexibility [2]. However, it is reported that welding of aluminum parts manufactured by PBF-LB leads to porous weld seams [4, 5], especially compared to weld seams in sand- or pressure die-cast parts [6]. Pores in the weld seam have several undesirable effects such as lowering the mechanical strength [7, 8] or fatigue strength [3] of the joint and lowering the electrical conductivity, which is paramount for e-mobility applications [9].

Pore formation in laser beam welding has already been studied widely and different pore formation mechanisms such as keyhole instabilities and entrapment of shielding gas have been identified [10–12]. Especially for laser welding of aluminum and aluminum alloys, hydrogen porosity is a frequent form of weld seam defect [13–16]. Miyagi et al. [17] proved in an experimental investigation that pores

✉ Steffen Kramer
steffen.kramer@ifsw.uni-stuttgart.de

[1] Institut fuer Strahlwerkzeuge IFSW, University of Stuttgart, Pfaffenwaldring 43, 70569 Stuttgart, Germany

[2] wbk Institute of Production Science, Karlsruhe Institute of Technology, Kaiserstraße 12, 76131 Karlsruhe, Germany

[3] Chair for Laser Technology LLT, RWTH Aachen University, Steinbachstraße 15, 52074 Aachen, Germany

[4] Fraunhofer Institute for Laser Technology ILT, Steinbachstraße 15, 52074 Aachen, Germany

[5] Institute of Materials Physics, Helmholtz-Zentrum Hereon, Max-Planck-Str. 1, 21502 Geesthacht, Germany

occurring during laser welding of aluminum materials mainly contain hydrogen. The hydrogen is believed to originate from moisture on the part or in the ambient atmosphere as for the laser welding of conventional aluminum an early investigation of Kutsuna et al. [18] showed that moisture on the specimen surface increases the weld seam porosity. Gou et al. [19] observed a similar impact of the ambient humidity during aluminum laser welding.

Several studies showed that aluminum alloy parts manufactured by PBF-LB are especially prone to pore formation in laser welding [2, 4–6, 8, 20]. Cui et al. [4] and Zhang et al. [6] conducted laser welding experiments with AlSi10Mg parts manufactured by PBF-LB and casting. Despite constant boundary conditions the PBF-LB manufactured part showed a 6–26 times increased weld seam porosity compared to the cast part. It is believed that this increase in porosity is caused by hydrogen which stems from powder moisture and is captured inside the part during PBF-LB [2, 6].

Recent studies investigated different possibilities to reduce the porosity in weld seams of aluminum parts. Cui et al. [4] investigated a laser melting deposition process, filling the weld gap layer-wise with powder material during the welding process. Sun et al. [21] used a laser with a variable core-ring intensity distribution for welding and managed to reduce the weld seam porosity by 40% withan optimized intensity distribution. In a study by Wang et al. [22] chemical cleaning and mechanical polishing were used as surface treatment before welding. This resulted in a 93% decreasein weld seam porosity but also in a decrease in welding depth. Chen et al. [2] investigated laser welding of AlSi10Mg parts manufactured by PBF-LB with increased ambient pressure. Porosity and pore size were significantly reduced by welding under an increased pressure of 0.4 MPa.

Although all listed approaches improve the weld seam quality, the root cause of the porosity formation, hydrogen, is not addressed. Furthermore, these techniques often need a complex infrastructure or hamper the productivity due to a reduced welding speed. Therefore, this paper investigates the formation mechanisms of hydrogen pores and an approach to prevent hydrogen pore formation during welding of aluminum PBF-LB manufactured parts.

1.1 Formation mechanisms for hydrogen porosity

The formation of hydrogen pores is well investigated for the casting of aluminum and aluminum alloys. For a hydrogen pore to form, the partial pressure of hydrogen

$$p_{H_2} > p_{amb} + p_{hy} + \frac{2\sigma}{r} \tag{1}$$

in the melt has to exceed the sum of the ambient pressure (p_{amb}), hydrostatic pressure of the melt (p_{hy}) and the pressure caused by the surface tension (σ) and the pore radius (r) of the pore nucleus [14].

It is widely recognized that homogeneous pore nucleation in the free-flowing melt is not possible [23, 24]. Due to the small radius of a free-flowing pore nucleus, the necessary partial pressure of hydrogen and thereby the necessary hydrogen concentration would be unrealistically high [15] and hydrogen pore formation during casting has been documented for hydrogen contents as low as 0.15 ml/100 g [25]. Therefore, most investigations propose either:

- a locally limited homogeneous pore nucleation in areas with increased hydrogen concentration, or
- some kind of heterogeneous pore nucleation, meaning that hydrogen pore nucleation occurs on or between certain surfaces or substrates and thereby effectively reducing the necessary partial pressure.

The three most commonly proposed hydrogen pore formation mechanisms are depicted in Fig. 1.The first proposed mechanism is interdendritic pore formation [25–27] and is depicted in Fig. 1a). Hydrogen is rejected by the progressing solid phase because of the significantly lower solubility of hydrogen in solid aluminum compared to the liquid state, and agglomerates in the melt. This leads to a locally increased hydrogen concentration in front of the solid/liquid (S/L) interface and especially between the dendrites when compared to the average hydrogen concentration in the free-flowing melt. The locally increased hydrogen concentration is causing the partial pressure of the hydrogen to exceed the pressure threshold, thereby enabling pore nucleation at the base of the dendrites. Pore nucleation and growth is facilitated by a simultaneous drop in the hydrostatic pressure of the melt in the mushy zone. This is due to the volume change caused by the shrinking of the material during solidification and subsequent melt flow into the interdendritic space [28, 29]. The surface of the dendrites is well wetted with melt which would cause pore nuclei to develop contact angles close to 180° when attached to the dendrite surface [14, 30]. The high contact angle translates to a small pore radius r, and following Eq. 1 thereby increasing the necessary hydrogen pressure for pore nucleation. Campbell [30] therefore assessed that nucleation occurs primarily in the liquid phase. Pore nuclei grow by absorbing the hydrogen from the surrounding melt and can occasionally leave the mushy zone at the S/L interface and float into the weld pool when above a certain size [31]. The pore shape and size is not necessarily limited by the adjacent dendrites as the pressure in the pore can bend and deform the surrounding material [27].

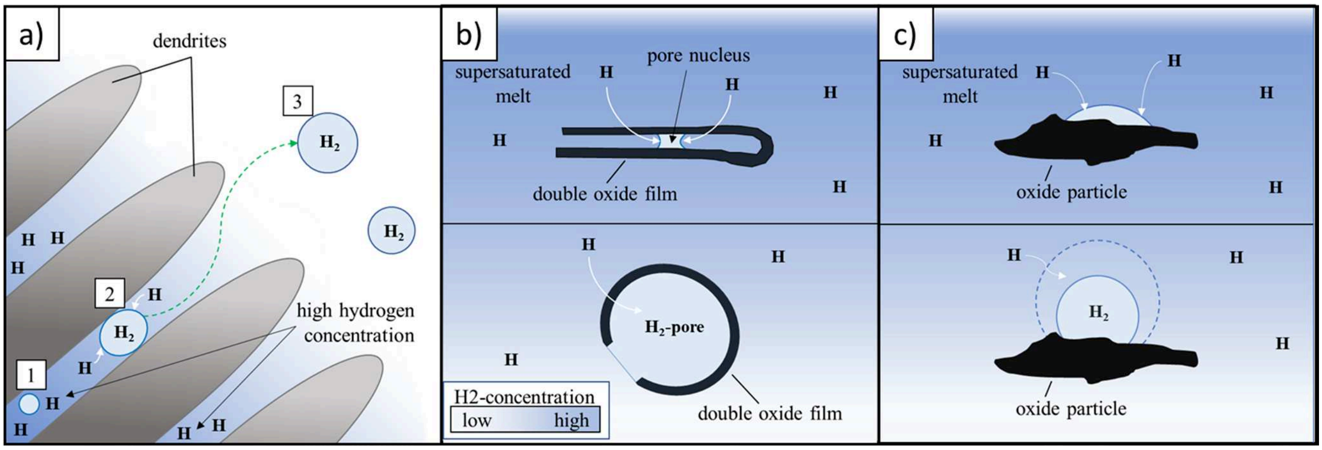

Fig. 1 Pore formation mechanisms in literature: a) interdendritic pore formation with (1) pore nucleation, (2) pore growth and (3) pore detachment. b) pore formation between double oxide films. c) pore formation on oxide particles

The second proposed mechanism is the pore formation between double oxide films ("bifilm-theory". Figure 1b)) [23, 30, 32–34]. Oxide films which build on the surface of the aluminum melt due to remaining oxygen in the ambient atmosphere are entrapped and folded by the movement of the melt, building a bifilm particle. These non-metallic inclusions possess a significantly lower wettability compared to dendrite surfaces. Pore nuclei on these surfaces develop a small contact angle and consequently a large radius which in turn drastically decreases the surface tension of the pore nucleus. Hence, pores nucleate between the folded oxide films due to the significantly reduced necessary hydrogen pressure and start to expand. Pore defects based on this mechanism were for example reported by Cao & Campbell for Al-Si casting parts [35].

While most fundamental research on hydrogen pore formation in aluminum is based on casting processes, several studies also explored the hydrogen pore formation for welding of aluminum materials. Cross et al. [14] investigated the hydrogen pore formation during laser welding and concluded, that the probability for homogeneous pore formation in the free-flowing melt pool is negligible during laser welding. Pore formation was assessed to most likely happen on non-metallic inclusions due to the low wettability of these particles by the melt. Interdendritic pore formation was not considered in this work. Trometer et al. [36] suggested that during laser welding of aluminum the natural oxide layer on the surface of the part is broken up. Fragments of the oxide layer then distribute in the weld pool during the laser welding and act as pore nucleation sites. (Fig. 1c)) This third proposed mechanism does not include a double oxide film as presented by the "bifilm theory". Gu et al. [37] simulated the dendrite growth coupled with the formation of hydrogen pores for the laser welding of a AlCu-alloy. The simulation shows the formation of hydrogen pores in the interdendritic region and an increased hydrogen concentration in the melt surrounding the dendrite tips. An experimental validation confirmed that an increase in cooling rate leads to a decrease in pore size and an increase in solute trapping of hydrogen.

The literature review clearly shows that while there are multiple theories on the hydrogen pore formation mechanism during laser welding of aluminum materials, knowledge is limited.

1.2 In-process laser drying during PBF-LB

Investigations showed that the powder material used in PBF-LB quickly picks up moisture from the ambient humidity due to the large surface to volume ratio [38]. During PBF-LB the moisture is split and oxygen and aluminum build stable aluminum oxides,

$$3H_2O + 2Al \rightarrow Al_2O_3 + 3H_2 \tag{2}$$

while hydrogen is absorbed into the aluminum melt due to the high solubility of hydrogen in liquid aluminum,

$$H_2 \rightarrow 2H_{abs.} \tag{3}$$

The high cooling and solidification rates of the PBF-LB process lead to entrapment of hydrogen in the material during solidification [39]. While most of the hydrogen remains in atomic form in the supersaturated Al-phase, part of the hydrogen forms small gas pores during the PBF-LB process [40]. During a consecutive heat treatment, especially at solution heat treatment temperatures above 500 °C [41], hydrogen diffusion leads to the formation of additional pores as well as to the expansion of already existing pores ("hydrogen blistering") [42]. This effect can lead to significant dimensional changes of PBF-LB manufactured parts,

Table 1 Chemical composition of AlSi10Mg powder material in %

Si	Mg	Fe	Mn	Ti	Zn	Cu	Al
9.8	0.35	0.18	0.01	0.03	0.01	< 0.01	Bal.

thereby affecting the parts quality [43]. Moreover, hydrogen embrittlement is a key factor enhancing stress corrosion of aluminum parts [44, 45]. An experimental study by Gatto et al. [46] showed an increased corrosion for AlSi10Mg parts manufactured by PBF-LB compared to cast parts. Therefore, multiple studies investigated possibilities to reduce the hydrogen content or hydrogen pores inside PBF-LB manufactured aluminum parts.

Weingarten et al. [39] investigated the formation of hydrogen pores during PBF-LB and proposed in-process laser powder drying as a new method to effectively reduce powder moisture and thereby hydrogen porosity in PBF-LB parts. This process uses a defocused laser beam to locally and layerwise heat the spreaded powder in the PBF-LB process chamber and evaporate moisture. An experimental study by van Cauwenbergh et al. [47] compared in-process laser drying with hydrogen outgassing and hydrogen solute trapping with regard to the amount of pores in a PBF-LB part. While hydrogen outgassing aims at releasing hydrogen into the inert atmosphere by slowing down the solidification process it also led to the formation of large process pores. Hydrogen solute trapping prevents the release of hydrogen completely with a fast solidification process resulting in a part supersaturated with hydrogen and only few pores. As the trapped hydrogen would outgas and lead to intense porosity in a consecutive welding process due to the slower solidification rate of the welding process, hydrogen solute trapping is also not suitable. Lubkowitz et al. [48] conducted experiments to compare vacuum drying and furnace drying with in-process laser drying, proving the latter to be the most effective strategy to minimize powder moisture and the formation of oxide layers on the powder particles.

The aim of this paper is to investigate and describe the formation of hydrogen pores when welding PBF-LB manufactured AlSi10Mg parts using in-situ high speed X-ray imaging. In a second step, in-process laser drying during PBF-LB is used, to reduce the hydrogen content of the manufactured specimens as a strategy to mitigate the formation of hydrogen pores in the subsequent welding process. The prepared specimens are welded and the hydrogen pore formation is compared with standard PBF-LB specimens. The impact of different drying intensities on the resulting weld seam porosity is investigated. Based on the results, a theory for the formation of hydrogen pores during welding of AlSi10Mg PBF-LB-manufactured parts is proposed.

2 Materials and methods

The AlSi10Mg powder material used for specimen production had a particle size between 20 and 63 µm with an average diameter of 42.14 µm and was supplied by m4p material solutions GmbH (Magdeburg, Germany). The chemical composition of the powder material is listed in Table 1.

In-process laser powder drying as presented in [39] was used to locally dry the spreaded powder before melting the desired area and thereby manufacturing batches of specimens with reduced hydrogen content. The procedure is schematically depicted in Fig. 2. In a first step (Fig. 2a)), the area of the specimen is irradiated with a defocused laser beam using a reduced laser power compared to the actual PBF-LB process. This leads to heating of the powder, the moisture is evaporated and taken away by the inert gas flow inside the process chamber. The reduced intensity prevents the melting of the powder particles and therefore prevents the evaporated moisture to be captured by the melt. In a second step (Fig. 2b)), the laser beam is focused on the surface of the powder layer, melts the dried powder material and thereby generates the desired part geometry.

For the laser drying process step the focal plane is shifted up by 10 mm thus defocusing the laser to a spot diameter of 230 µm on the powder layer surface. Four different parameter sets for laser drying, taken from [48], were tested and are listed in Table 2. The line energy is used to characterize the heat input

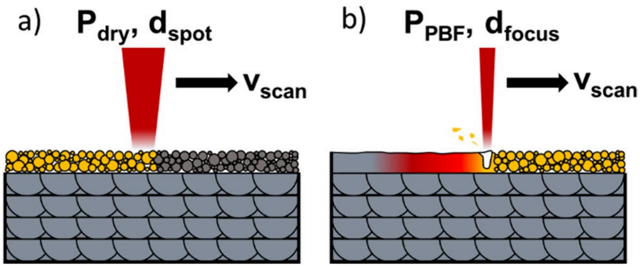

Fig. 2 Schematic depiction of the PBF-LB process steps with in-process laser powder drying: (**a**) powder drying using a defocused laser beam (**b**) melting the dried powder using a focused laser beam

Table 2 Parameter sets for laser powder drying

Laser powder drying parameter set	Laser power P_{dry} in W	Scanning speed v_{scan} in mm/s	Hatch distance in µm	Line energy (= P/v) in mJ/mm
D1	25	1037	160	24
D2	38.8	1288	155	30
D3	75	1500	155	50
D4	75	1000	155	75

for the powder drying process and is calculated as the quotient of laser power and scanning speed. Reference specimens were manufactured alongside without in-process laser powder drying.

Specimens were manufactured on a SLM 280 HL machine from Nikon SLM Solutions AG (Luebeck, Germany) using Argon as an inert gas. The machine is equipped with a fiber laser with a wavelength of 1070 nm. The beam profile was measured according to DIN EN ISO 11146-2 with a M^2 of 1.33, a Rayleigh length of 3.77 mm and a focus diameter of 83 µm on the powder bed surface. The PBF-LB process parameters (Table 3) combined with a 67° rotation of the scanning pattern between the layers reliably produce specimens with a relative density of > 99.5%. All manufactured specimens had a size of 50 × 30 × 2 mm³.

The welding experiments were performed at the "Deutsches Elektronen-Synchrotron" (DESY) X-ray radiation source PETRA III at beamline P61A, operated by the Helmholtz Centre Hereon in Hamburg, Germany. In-situ X-ray imaging of laser welding processes using synchrotron radiation was introduced in 2012 by Yamada et al. [49] and has since been established for in-situ investigations on melt flow [50], pore formation [17, 51] or welding capillary behavior [52]. In recent years this method was even adapted for in-situ observations of the PBF-LB process [53]. The experimental setup for capturing in-situ X-ray images of the welding process is schematically depicted in Fig. 3. A collimated, white X-ray beam radiates through the process zone of the sample. The intensity of the X-ray radiation after the sample is based on the local attenuation of the X-ray beam in the welding specimen. As the attenuation during the passage through the specimen is weaker for gaseous material such as pores, bubbles or the welding capillary these features become visible as brighter areas compared to the denser aluminum material. In addition, diffraction of the X-rays and the associated interference occur at phase boundaries. This leads to black edges at the transition between gas and solid or liquid. The X-rays are transformed into visible light by a Cerium doped Lutetium Aluminum crystal (Ce:LuAG) scintillator with a thickness of 600 µm. This light is mirrored and captured by a high-speed camera (iSpeed 727 by ix Cameras, UK) with a frame rate of 50 kHz. The observed section is 1.6 × 2.1 mm² with a resolution of 383 px/mm. The image processing includes a flat-field correction to exclude possible defects from the scintillator, imaging system or camera and to mitigate the intensity distribution of the brightness of the X-ray beam. This is followed by a Kalman filter operation to reduce noise and a fast Fourier transform to mitigate periodical features generated by the high-speed camera sensor. To improve the X-ray image quality the surface roughness of all specimens was reduced by grinding and polishing.

Table 3 PBF-LB process parameters for specimen production

Parameter	Value
Laser Power P_{PBF}	350 W
Scanning Speed v_{scan}	1150 mm/s
Hatch Distance h	170 µm
Layer Thickness t	50 µm

Fig. 3 Experimental setup for capturing in-situ X-ray images of the laser welding process

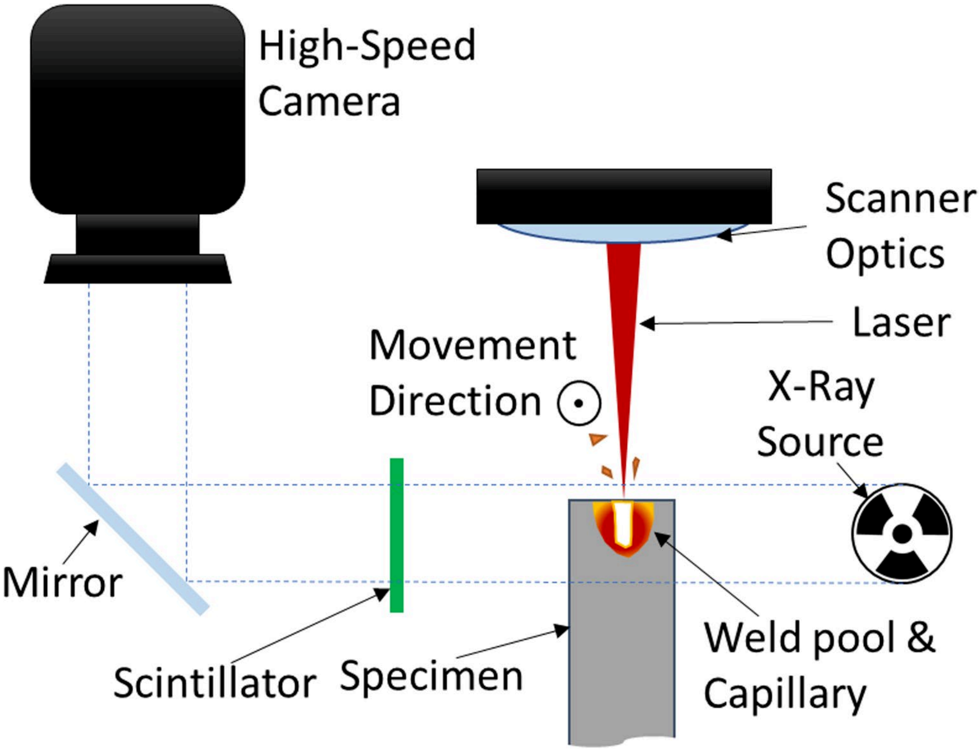

Laser welding was performed using a single mode fiber laser (Coherent, USA) with a wavelength of 1070 nm (M^2 = 1.31), laser power of 1.5 kW and the focal plane was set 4 mm above the specimen surface, resulting in a laser spot size of 187 µm on the specimen surface. Laser welding parameters were maintained for all welding experiments and all specimens, reference specimens and laser-dried specimens. The laser beam was moved over the specimen surface with a feed rate of 400 mm/s using a scanner optic. The laser parameters were set to result in a U-shaped capillary, which is known to be a stable capillary shape [54], therefore preventing the formation of any process pores and ensuring almost all of the observed pores are generated inside the weld pool during cool down. As common for remote laser welding, no shielding gas was used during laser welding.

For every weld seam six cross-sections were prepared, polished and etched using NaOH as etchant. The porosity of the weld seam and the base material was evaluated using binarized optical microscope images and the particle analysis tool provided by ImageJ. Single pores were further investigated with a Helios NanoLab600 (FEI Company, USA) scanning electron microscope (SEM) equipped with an Aztec EDX Ultim Max energy-dispersive X-ray spectroscopy (EDS) unit (Oxford Instruments, UK). The microstructure was investigated using a JSM-6010 LV SEM (Jeol, Japan). The hydrogen content of the specimen’s material was measured using carrier gas hot extraction. Three material samples of the reference material and D4 material with a mass of 0.8–0.9 g each and polished surfaces were used for hydrogen content measurement.

3 Results

3.1 Formation of hydrogen porosity

The formation of hydrogen porosity was evaluated for laser welding of PBF-LB manufactured specimens without applying the in-process laser drying process (“reference specimens”).

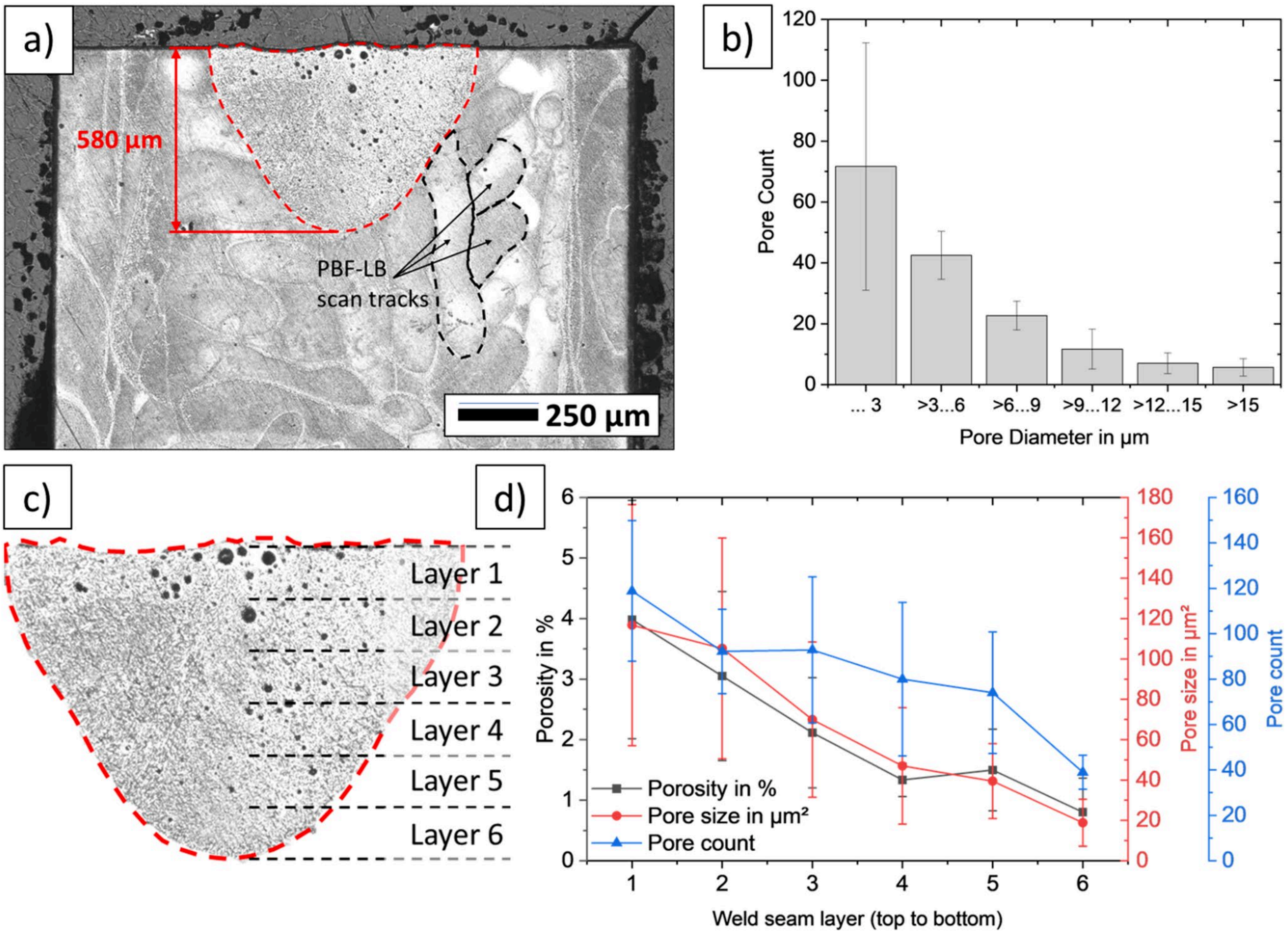

(**a**) Cross-section of a weld seam containing numerous pores (reference material). The shape of the weld seam is outlined by the dashed red line. Laser welding parameters see Table 4. (**b**) Average size distribution of the pore diameter of pores inside the weld seam (reference material) Error bars: standard deviation. (**c**) Schematical depiction of the layerwise separation of the weld seam cross-section, to measure local porosity deviations. (**d**) Development of the average porosity, pore size and pore count over the depth of the weld pool

Table 4 Laser welding parameters

Laser power	Feed rate	Spot diameter on sample surface	Focus shift	M^2	Laser wavelength	Shielding gas
1.5 kW	400 mm/s	187 µm	4 mm	1.31	1070 nm	None

Figure 4a) shows an optical microscope image of the cross-section of a weld seam in a reference specimen. The welding process creates numerous pores inside the weld seam with increasing porosity towards the top and center of the weld seam. In the material surrounding the weld seam single scan tracks from the PBF-LB process are visible. Figure 4b) shows the average size distribution of pores inside the weld seam of the reference specimen. The porosity mostly comprises of pores smaller than 6 µm and only includes few pores larger than 15 µm. To further characterize the porosity and pore distribution, the weld seam was split in six horizontal layers (see Fig. 4c)). For every layer the average porosity as well as the average pore size and pore count was measured and the results are shown in Fig. 4d). The evaluation confirms the decrease in weld seam porosity from the top towards the bottom of the weld seam. The pore size and pore count decrease correspondingly.

The size of the weld pool was measured with the use of the X-ray images. It has a length of 3.3–3.5 mm and is longer than the section observed in a single image. Therefore, the complete weld pool and capillary is displayed by stitching four single frames of the X-ray image sequences with a time interval of 2.5 ms between each frame (Fig. 5).

The yellow line describes the shape of the weld pool and was determined by observing where bubbles moving inside the weld pool start to freeze, since the actual S/L interface is not directly visible in the X-ray images. The depth of the weld pool measured from the X-ray image is 575 µm and corresponds well with the depth of the weld seam (580 µm) measured from the optical microscope image of the weld seam cross-section in Fig. 4a**)**. The shape of the capillary is highlighted with red and verifies the aspired U-shape, resulting in a stable capillary. An exemplary temporal sequence of the stable capillary shape is provided in appendix A1. Consequently, the weld pool behind the capillary does not contain any process pores caused by instabilities of the vapor capillary. The base material, however, naturally contains a certain amount of porosity from the PBF-LB process. These pores can be categorized as "gas pores" due to their small diameter and spherical shape [39]. As indicated by the Arabic numbers in Fig. 5, gas pores in the base material can either be:

1) on the side of the weld seam and not be affected at all, but still visible in the X-ray images as unmoved pore defects,
2) picked up by the weld pool and escape the melt due to the buoyance,
3) or be picked up by the weld pool, remain in the weld pool, grow e.g., due to the thermal expansion of the contained gas and/or due to fusion with other pores and freeze in the solidifying melt.

Pores which directly meet the capillary dissipate and the contained gas is presumably released into the environment. However, towards the end of the weld pool numerous bubbles occur inside the weld pool, highlighted with

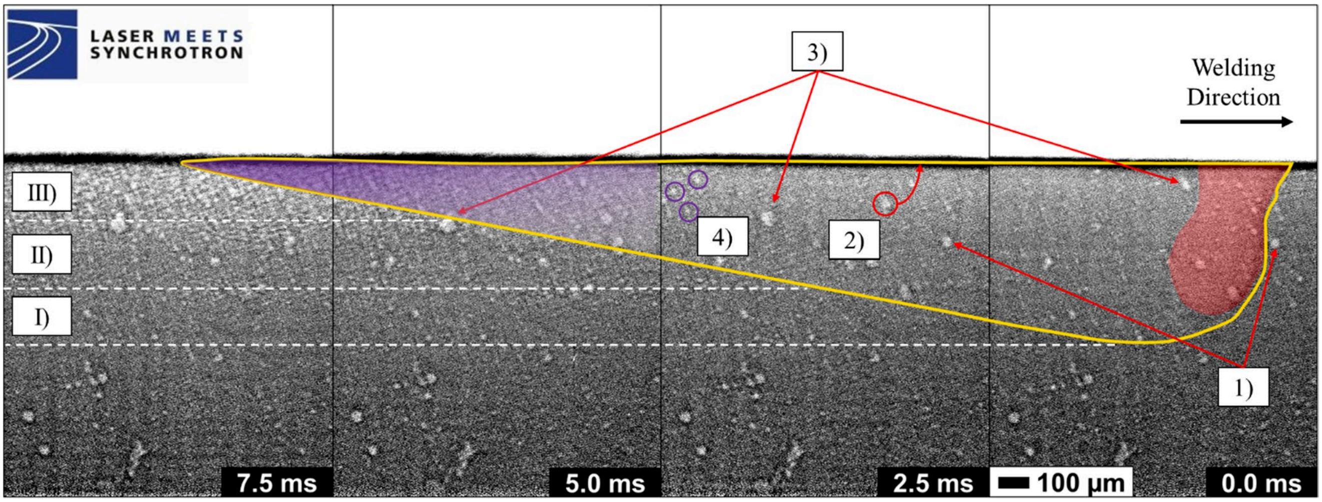

Fig. 5 Stitched image sequence of X-ray images showing the weld pool and capillary (reference material). The shape of the weld pool is indicated by the yellow line, the capillary is highlighted in red. Laser welding parameters see Table 4. The corresponding high-speed recording of the reference material is provided in the supplementary materials (Online Resource ESM 5).

purple shading, resulting in pores in the weld seam. By comparing the depicted frames, it is evident that along the welding direction the first bubbles of this kind can be found in the middle of the weld pool (see 4), purple circles) while the front of the weld pool is free of bubbles except the ones already present in the materials as e.g. 1)–3). As these newly formed bubbles at 4) are neither process pores nor pores from the base material, it is believed that these bubbles form through diffusion and accumulation of hydrogen. Along the weld pool depth, the weld pool can be separated in three different zones (I-III) depending on the pore formation characteristics, where the transition between the zones is smooth. No pore formation can be observed at the bottom of the weld pool (zone I). In zone II few pores form at the solidification front at the end of the weld pool and expand but no bubbles are present in the weld pool. In zone III pores are much more numerous at the S/L interface at the end of the weld pool. The porosity increases towards the end of the weld pool to a point where it is not possible anymore to identify single pores in the X-ray images. This is due to the small diameter of the pores (<4 px) in this region and the overlapping of multiple pores in the direction of the X-ray beam, making a quantitative analysis of the X-ray images impossible. The increased porosity towards the top of the weld pool however is confirmed by the cross-section in Fig. 4a) and Fig. 4b) demonstrates the large number of small pores inside the weld seam. Also, in zone III bubbles can be observed further away from the S/L interface floating inside the weld pool (see (4)). These bubbles have a diameter of 5 to 6 pixel in the highspeed camera recordings, which equals 13–16 µm and corresponds well with the size of the largest pores measured in Fig. 4. The agglomerated bubbles near the S/L interface show no general movement but rather solidify at or near the formation site.

Single pores inside the weld seam were investigated with optical microscopy (see Fig. 6a & b) and SEM (see Fig. 6c). The investigated pores have a spherical shape and show no signs of aluminum oxide particles or oxide layers as these would clearly stand out from the base material as shown in microscopic images of oxide particles by [35, 36]. This is confirmed by the EDS elemental analysis of the pore (see Fig. 6d)) which shows no oxygen concentrations inside the pore. The only oxygen-containing particles are agglomerations of the colloidal silicon dioxide of the polishing suspension. The EDS analysis further shows that the typical Si-network structure of fast-solidifying AlSi10Mg is maintained inside the pore [55]. Magnesium is evenly dispersed inside the material. The microstructure inside and outside the weld seam consists of a Si-rich network surrounding the Al-phase. The coarser microstructure inside the weld seam (Fig. 6e)) compared to the base material (Fig. 6f)) is due to the slower cooling rate of the laser welding process compared to the PBF-LB process.

3.2 Reduction of hydrogen porosity

In addition, laser welding with the same process parameters was applied to the material which was manufactured with an additional in-process laser drying step during PBF-LB (D1-D4). The line energy used for the laser drying process was varied between 24 and 75 mJ/mm. Polished cross-sections of the resulting weld seams are shown in Fig. 7. For low line energies during the in-process laser drying (24 & 30 mJ/mm, Fig. 7a & b)) the weld seam still contains numerous pores which are distributed at the top of the weld seam. With an increased line energy (50 mJ/mm, Fig. 7c)) the number of pores decreases drastically. The maximum line energy (75 mJ/mm, Fig. 7d)) enables a weld seam containing no macroscopic pores. The in-process laser powder drying does not influence the shape or size of the weld seam, as these remained constant for all experiments.

The relative porosity of the weld seam and the corresponding base material was evaluated using binarized microscope images. For every material configuration 5–6 cross-sections were evaluated. Results for the porosity measurement are summarized in Fig. 8a). The porosity of the base material remains constant for the different laser-dried materials and is comparable to the porosity in the reference material (line energy 0 mJ/mm). The average weld seam porosity is the highest for the reference material and slightly decreases for lower line energies (24–30 mJ/mm). The high deviation in porosity for all weld seams is caused by the occasional presence of larger pores in the weld seam as seen in Fig. 7c). Based on the observations from the in-situ X-ray imaging (described in Sect. 3.1), these pores are believed to originate from the base material and solidified in the weld seam (see Fig. 5, number 3)). The weld seam porosity significantly decreases for higher line energies of the drying process. For the maximum line energy (75 mJ/mm) the average weld seam porosity is equivalent to the already existing porosity of the base material. Figure 8b) shows the average circularity of the pores inside the weld seam and the base material. Pores inside and outside the weld seam tend to have a roundish shape with a circularity between 0.7 and 0.8. Considering the significant standard deviation, the circularity inside and outside the weld seam can be deemed as constant for all investigated line energies as well as the reference material. The results for the weld seam porosity presented in Figs. 7 and 8 show that the in-process laser drying step was successfully applied to reduce the resulting weld seam porosity in the laser welded parts.

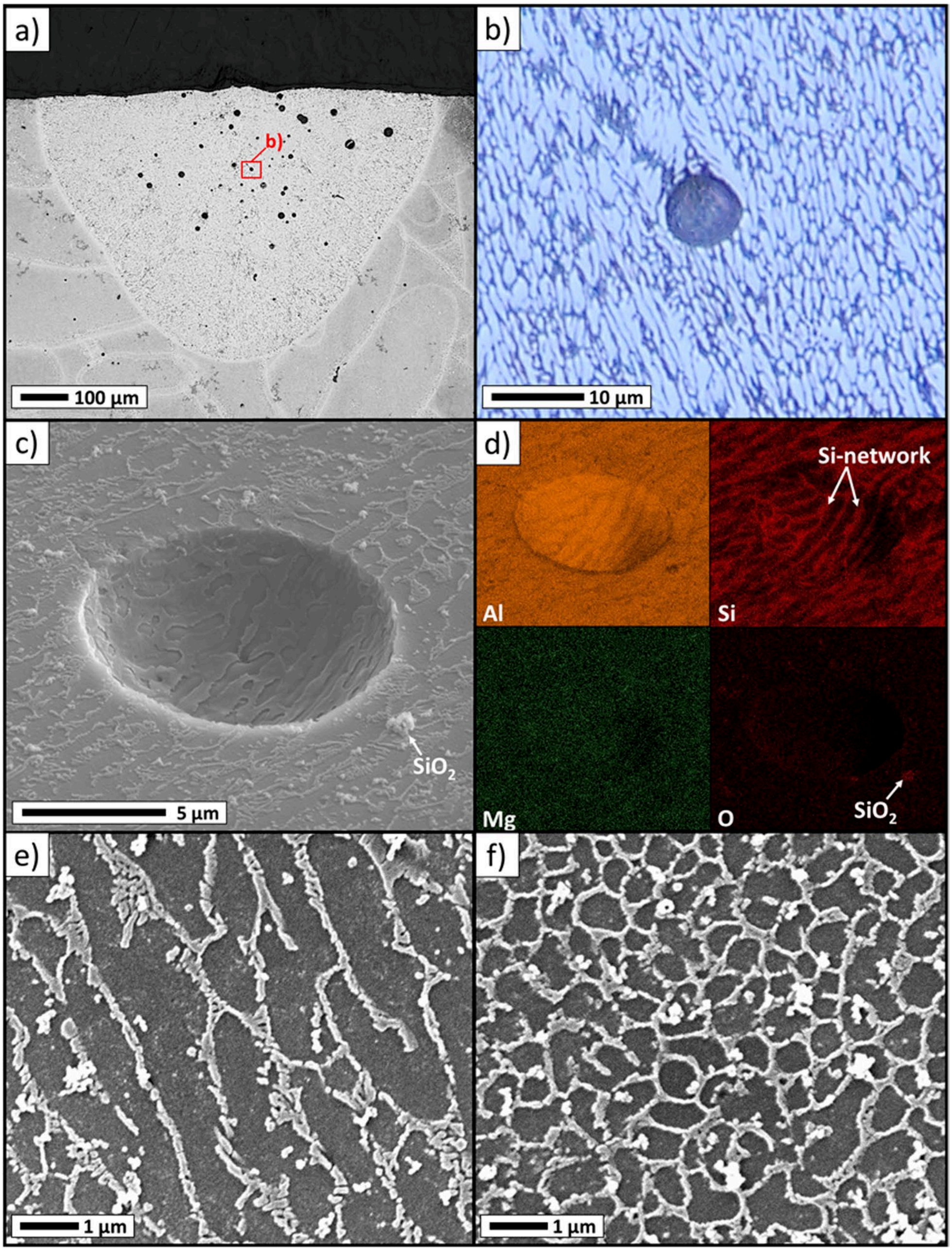

Fig. 6 (**a**) Optical microscope image of the polished cross-section of a weld seam (reference material) (**b**) Detailed optical microscope image of an exemplary hydrogen pore and surrounding microstructure, etched with NaOH (**c**) SEM image of an exemplary pore inside the weld seam; tilted towards the EDS detector to achieve a sufficient signal for elemental analysis (reference material) (**d**) EDS elemental analysis of the pore and surrounding material (**e**) typical microstructure inside the weld seam (**f**) typical microstructure of the base material

The hydrogen content of the base material was measured exemplary for the reference material as well as for the laser-dried material D4 (line energy 75 mJ/mm) by carrier gas hot extraction. For the reference material the hydrogen content is 5.71 (±0.56) ml/100 g and for the laser-dried material D4 it is 4.26 (±0.23) ml/100 g. This is a significant 25% decrease in hydrogen content achieved by the in-process laser drying. The corresponding X-ray image sequence (Fig. 9) illustrates that no pores form during laser welding of the laser-dried D4 material.

Figure 10 shows X-ray images of the different materials before and after the laser welding. It illustrates the local distribution of the pores in the weld seam. The distribution of the generated pores in the weld seam is identical for the reference material and the materials D1 and D2 (Fig. 10a-c)). The porosity increases gradually towards the top of the weld seam, which corresponds well with the porosity distribution observed from the optical microscope images of weld cross-sections presented in Fig. 4. The before/after X-ray images as well as the X-ray image sequences of all the materials

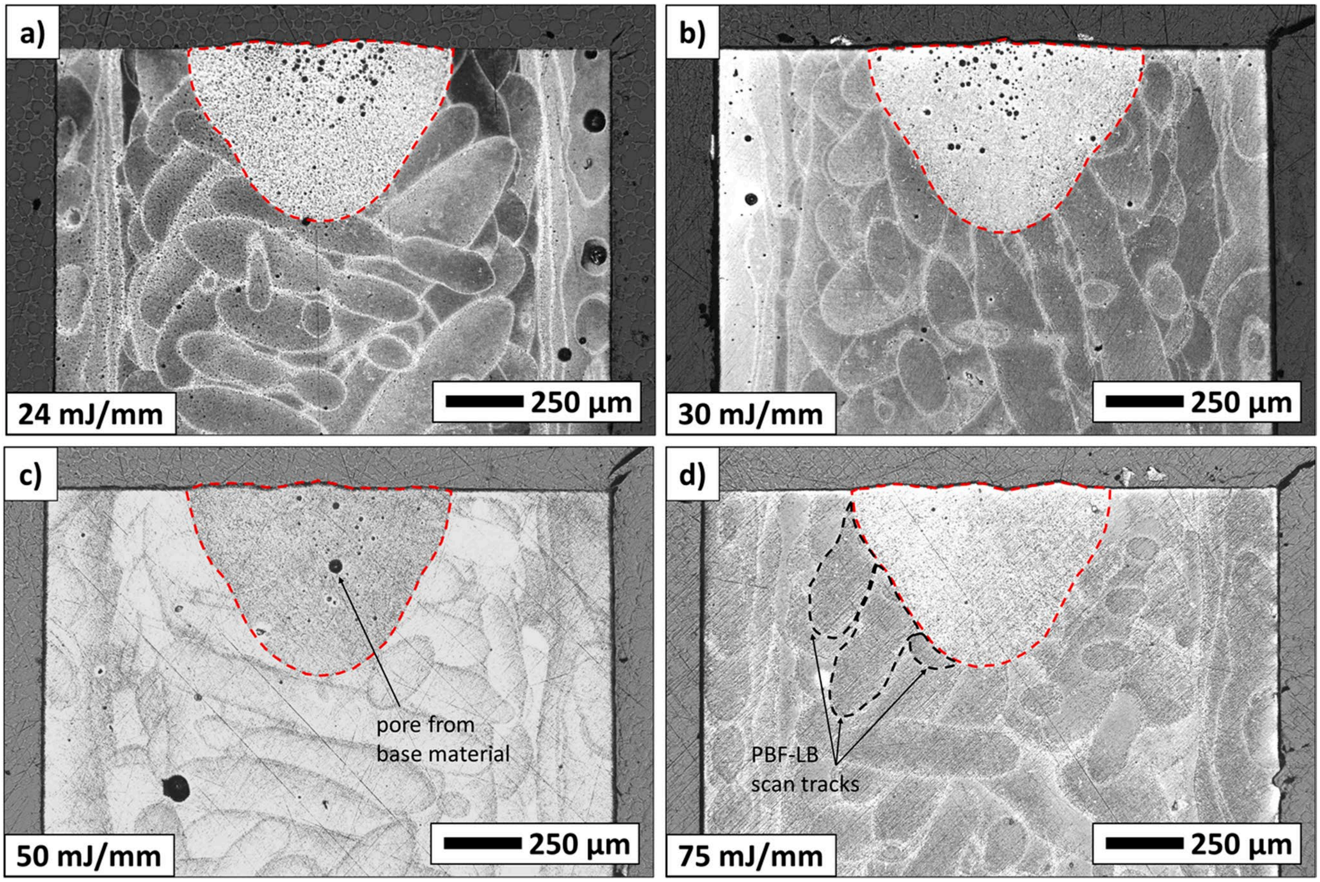

Fig. 7 Cross-sections of weld seams produced in laser-dried material. (**a**) D1, line energy: 24 mJ/mm, (**b**) D2, line energy: 30 mJ/mm, (**c**) D3, line energy: 50 mJ/mm, (**d**) D4, line energy: 75 mJ/mm. Laser welding parameters see Table 4

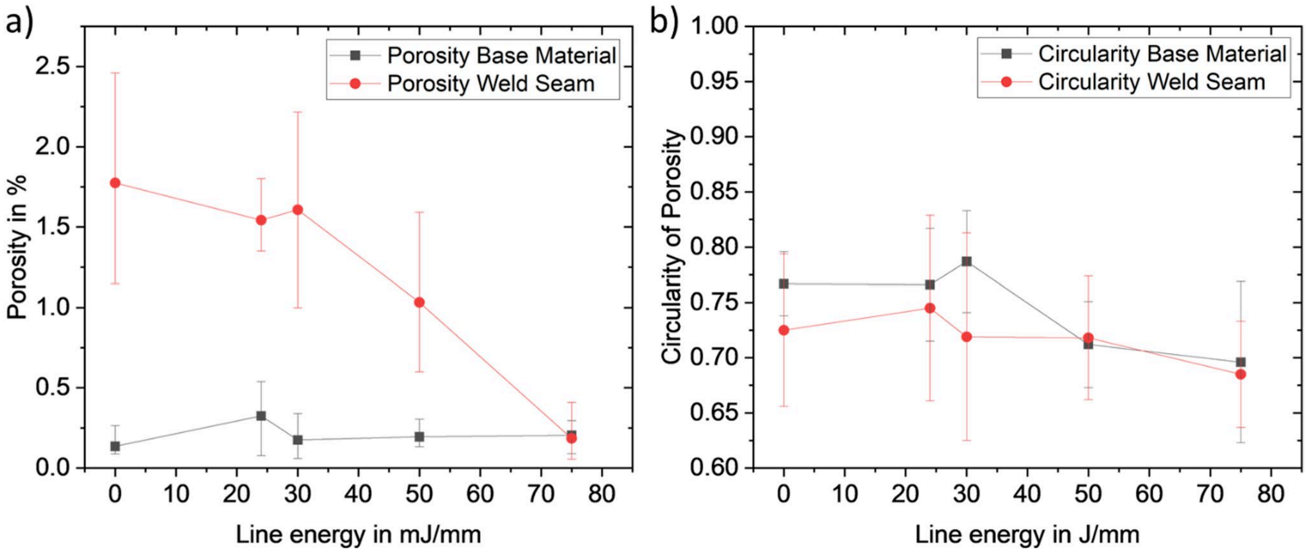

(**a**) Average porosity of the weld seam and the base material for different powder drying parameters. The reference material without laser powder drying is marked with a line energy of 0 mJ/mm Error bars: min/max error. (**b**) Average pore circularity inside the weld seam and in the base material. Error bars: standard deviation

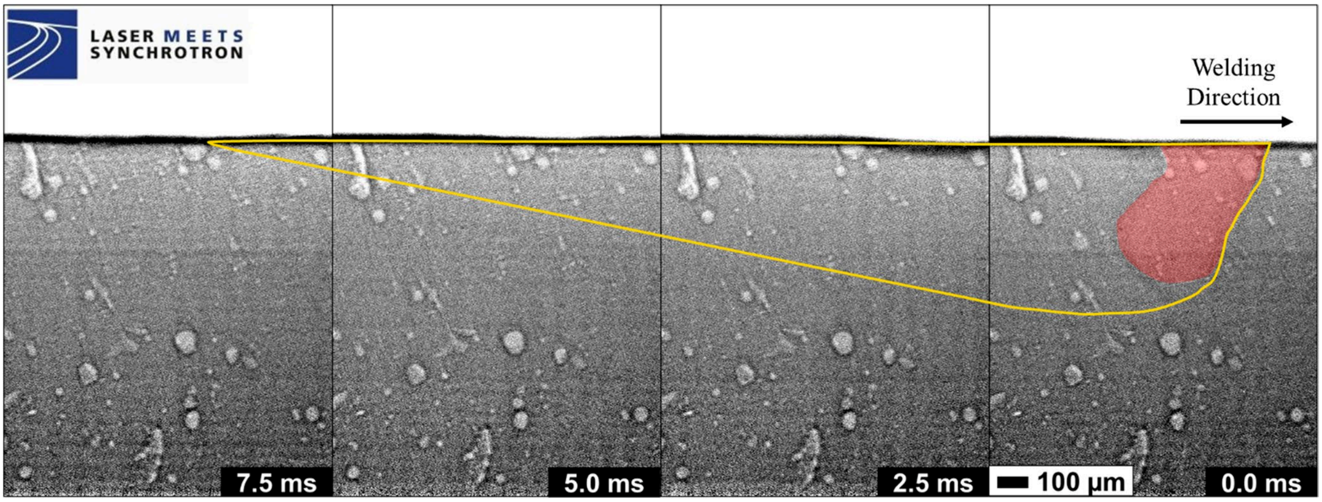

Fig. 9 Stitched X-ray image sequence for the laser welding of laser-dried material (D4). The shape of the weld pool is indicated by the yellow line, the capillary is highlighted in red. Laser welding parameters see Table 4. The corresponding high-speed recordings of the D1-4 materials (Online Resource ESM1-4) are provided in the supplementary materials.

(see appendix A2) show, that the in-process laser drying does not alternate the formation mechanism of pores in the weld seam but only the number and size of pores.

4 Discussion

All conducted experiments show that no process pores formed during laser welding, therefore process pores are ruled out as a possible origin of porosity. The X-ray images suggest that the majority of the pores form at or near the solidification front. For pure aluminum at solidus temperature (660 °C, 1.013 bar) the solubility of hydrogen in the liquid phase is estimated as 0.71 ml/100 g and 0.043 ml/100 g in the solid phase [56]. According to the hydrogen content measurement the hydrogen content of the reference material exceeds the solubility by a saturation factor of $S_{liq} = 8$ for the liquid phase and $S_{sol} = 133$ for the solid phase. The liquid aluminum in the weld pool is therefore supersaturated with hydrogen which causes the formation of hydrogen pores. For the laser-dried material D4 with a lower hydrogen content these factors reduce to $S_{liq} = 6$ and $S_{sol} = 99$, but still the hydrogen content is above the solubility limit for both, the solid and liquid phase. Nevertheless, the presented solubility values are determined for the equilibrium state of pure aluminum and alloying elements as well as non-equilibrium cooling can strongly influence the hydrogen solubility [56, 57]. The hydrogen solubility of the aluminum alloy AlSi10Mg is currently unknown. Therefore, it is possible that hydrogen capture due to the fast cooling and solidification during welding as well as an altered hydrogen solubility due to the alloying elements contribute to a pore free weld seam during laser welding of the D4 material despite a saturation factor $S_{liq} > 1$.

The hydrogen content of both, the reference material and the D4 material, is however much lower compared to the hydrogen content of 33.6 ml/100 g for unconditioned powder material which was measured by Weingarten et al. [39]. This indicates, that most of the hydrogen dissolves during PBF-LB either due to the heated build platform or during melting and solidification. Nevertheless, with the in-process laser powder drying the remaining hydrogen content in the PBF-LB parts can be further reduced significantly.

The optical microscope and SEM investigation of the pores in the weld seams did not show any signs of oxide particles or oxide films inside the pores. The nearly spherical shape and size of all investigated pores do also not comply with the irregular pore shapes of hydrogen pores caused by oxide films and oxide particles as presented by Cao & Campbell [35] and Trometer et al. [36] but is similar to hydrogen pores in PBF-LB manufactured aluminum parts [39, 45]. It is therefore believed that hydrogen pores did not form on oxide particles or between double oxide films in the weld pool when laser-welding PBF-LB manufactured AlSi10Mg parts. As the specimen surface was ground before laser welding the oxide layer resulting from the PBF-LB process was removed, consequently reducing the involvement of oxides in the pore formation. Hence, by process of elimination, hydrogen pores either formed in the interdendritic region at the solidification front, or by hydrogen diffusing into and expanding already existing microscopic pores in the weld pool.

Although the D4 laser-dried material surpasses the hydrogen solubility and the base material contains numerous pores, no indications for growth of these already existing pores was observed in the X-ray investigations. There is no increase in porosity inside the weld seam compared to the

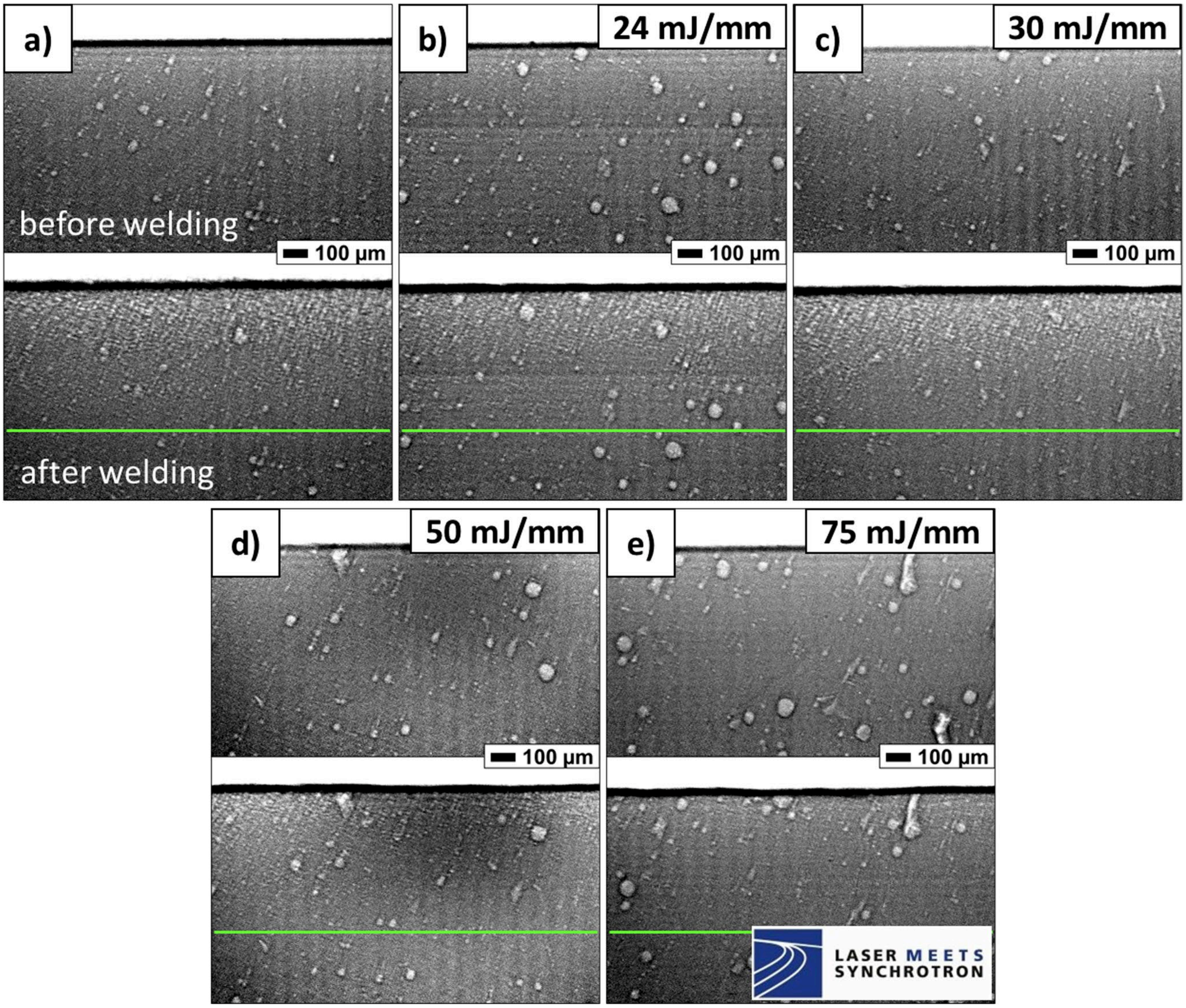

X-ray images of the specimens before (top) and after laser welding (bottom) for the different materials used. (**a**) reference material, (**b**) D1, line energy: 24 mJ/mm, (**c**) D2, line energy: 30 mJ/mm, (**d**) D3, line energy: 50 mJ/mm, (**e**) D4, line energy: 75 mJ/mm. The horizontal green line marks the depth of the weld pool

D4 base material as shown in Fig. 7d) and Fig. 8. Also, the X-ray images in Fig. 9 show no signs of growth for already existing pores. Therefore, the interdendritic pore formation at the solidification front is believed to be the dominant pore formation mechanism.

In the following, based on the presented results and in-situ X-ray observations, a possible explanation for the hydrogen pore formation mechanism is developed. As described in Sect. 1, hydrogen pores form if the local partial pressure of hydrogen in the melt exceeds the sum of the ambient pressure, hydrostatic pressure as well as the surface tension (see Eq. 1). As the solubility of hydrogen in liquid aluminum is 16 times larger compared to solid aluminum, hydrogen is rejected by the progressing S/L interface and agglomerates around the growing dendrites. The solidification path provides the necessary information to better understand the solidification process at the S/L interface in detail. The solidification path of AlSi10Mg is depicted in Fig. 11 and was calculated with Thermo-Calc 2023b and the provided aluminum alloy database TCAL8: Al-alloys v8.2. Calculations were done according to the Scheil-Gulliver model [58, 59], assuming rapid cooling which is typical for laser welding. As a comparison the solidification path under equilibrium conditions was also calculated (see Fig. 11; red, dashed line).

In the first phase of solidification primary α-Al solidifies (mass fraction solid fs = 0–0.23.23), which presumably corresponds to a quick growth of the dendrite tips. The

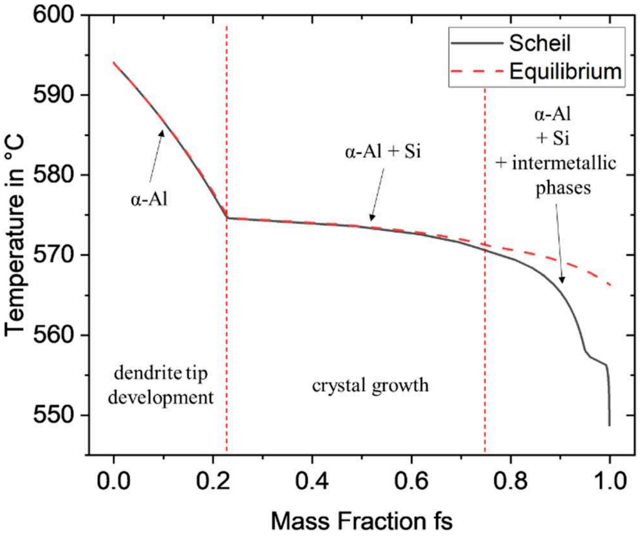

Fig. 11 Solidification path for AlSi10Mg calculated with Thermo-Calc 2023b according to the Scheil-Gulliver model (black line) and for equilibrium condition (red, dashed line)

majority of the material (fs = 0.23–0.75, indicated by the vertical, dotted red lines) solidifies in a second phase in a narrow temperature range of 570–575 °C. It is therefore in this phase, after the formation of dendrites, when the hydrogen concentration in the melt between the already solidified dendritic grains increases the most. This leads to a significantly higher hydrogen concentration between the dendrites compared to the dendrite tips. The comparison with the solidification under equilibrium conditions shows a significant under-cooling of the melt towards the end of the solidification. This can be attributed to the rapid cooling during laser welding. However, the majority of the solidification up to fs = 0.75 is similar for the rapid cooling (Scheil) and the equilibrium condition, probably due to the proximity to the eutectic composition with 12% silicon [60].

The straight incline of the rear of the weld pool, as seen in Fig. 5, relates to a constant solidification rate over the depth of the weld pool. As a constant solidification rate corresponds with constant formation conditions, a homogeneous pore distribution along the depth of the weld pool would be expected. However, the porosity distribution shown in Fig. 10 proves that more pores are found at the top while the root of the weld seam is often free of any hydrogen pores. The X-ray image sequence (Fig. 5) in turn shows that pores do not form at the bottom of the weld pool and rise to the top but are already formed at the top of the weld seam. Therefore, the pore distribution can only be explained with a three-dimensional analysis of the solidification of the weld pool (Fig. 12).

The highest porosity is found in zone III. Temperature gradients are typically low towards the end of the weld pool and near the surface and complete solidification takes more time compared to the bottom of the weld pool. This is illustrated by the distance between the liquidus isotherm T_{liq} and the solidus isotherm T_{sol} in Fig. 12. The slower solidification allows more hydrogen to agglomerate in front of the solidification front and allows pores to nucleate and grow. Additionally, the absolute volume of molten material and thereby the absolute amount of hydrogen in zone III is higher compared to zone I or II. This implies that the potential hydrogen concentration due to the agglomerating hydrogen in front of the S/L interface during solidification can also reach higher values in zone III compared to zones I and II. The high local hydrogen concentration leads to an increased partial pressure of hydrogen in the melt. As the solidification starts with α-Al dendrites, the silicon concentration in the melt between the dendrites increases, which in turn reduces the hydrogen solubility [61]. Both effects facilitate hydrogen pore formation. Pores are therefore mostly formed in the mushy zone (fs = 0.23–0.75) and do not flow in the weld pool as the melt does not flow between the dendrites to pick up the pores. However, the X-ray image sequence (Fig. 5) shows that some pores move with the melt flow. It is assumed that these pores do not nucleate between the dendrites but nucleate during the formation of the dendrite tips (fs = 0–0.23.23) and are picked up by the melt flow. The simulations by Gu et al. [37] suggest pore formation is possible in the early stages of solidification due to high hydrogen concentrations at the dendrite tips. Alternatively, these pores could exceed the critical size to escape the mushy zone as described by Yamamoto et al. [31].

In zone II the solidification time is reduced which leads to lower hydrogen concentrations at the S/L interface and a higher degree of solute hydrogen trapping. Pores are smaller and exclusively form in the mushy zone. In zone I temperature gradients are high as the surrounding base material conducts the heat. As illustrated by the small solidification region between T_{liq} and T_{sol}, the solidification time is extremely short which presumably prevents hydrogen to diffuse and agglomerate in front of the S/L interface. The hydrogen is captured in the material leading to a pore-free weld seam root supersaturated with hydrogen.

The lower hydrogen content in the laser-dried materials D3 and D4 consequently leads to an overall lower hydrogen concentration and a lower partial pressure of hydrogen in the weld pool and especially at the S/L interface in all three zones. This reduction prevents the partial pressure to cross the threshold for pore formation, even in zone III. Since the hydrogen content in the laser-dried material D4 is still above the solubility of hydrogen in aluminum at melting temperature, it is possible that for other welding parameters with overall slower solidification the hydrogen concentration in the solidification region is still sufficient for hydrogen pores to form.

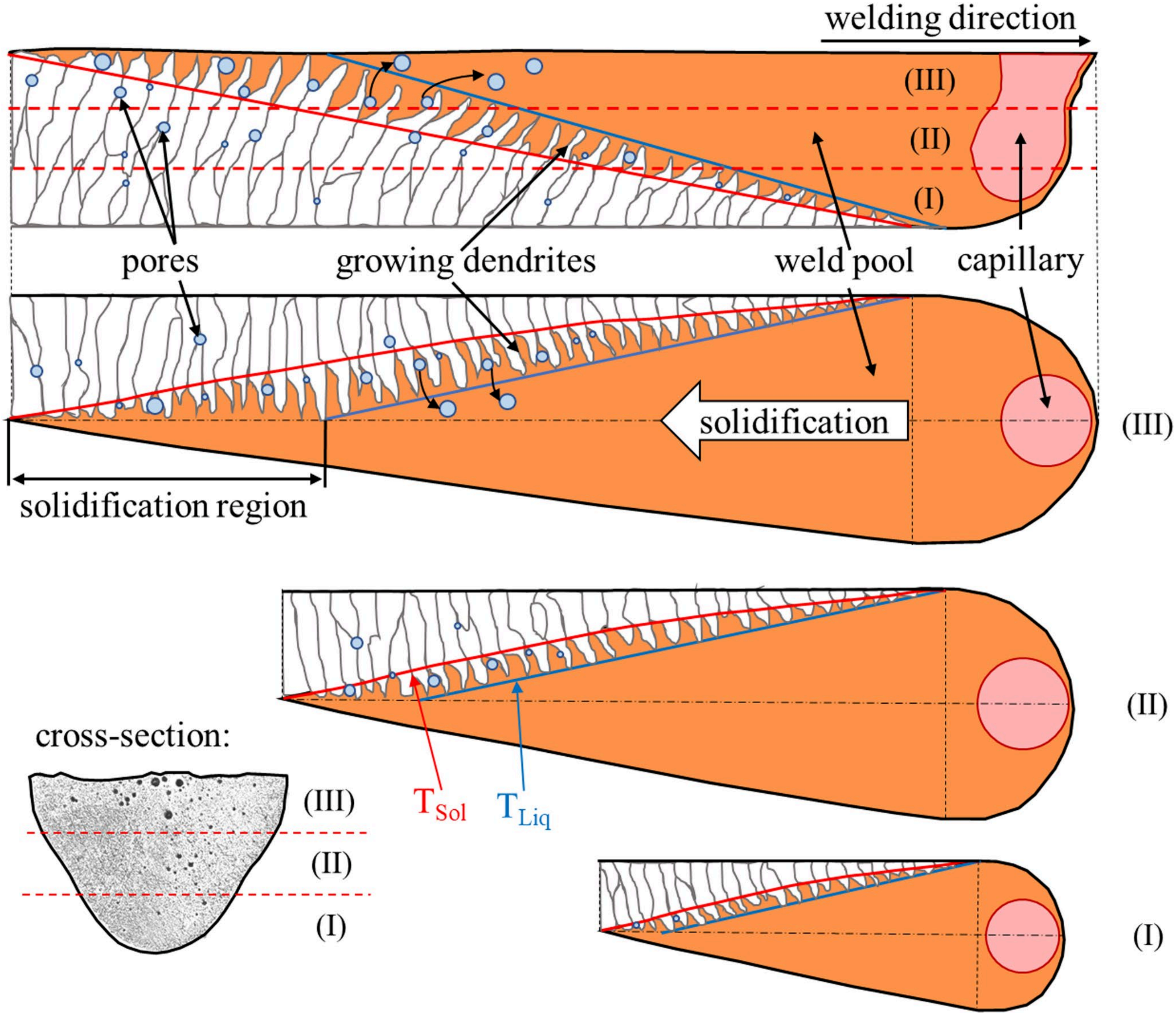

Fig. 12 Schematic depiction of the dendrite growth and the formation of hydrogen pores in the different zones (I-III, compare Fig. 5) of the weld pool

5 Conclusion

In this study the hydrogen pore formation for laser welding of PBF-LB manufactured AlSi10Mg parts was investigated by means of high-speed in-situ X-ray imaging. The measured hydrogen content of the reference part is 5.71 ml/100 g and exceeded the hydrogen solubility of pure solid aluminum at solidification temperature by a factor of 133. The results show, that hydrogen pore formation mainly occurs in the interdendritic region at the solidification front. Pores mainly form in the upper part of the weld pool, where the longer solidification time allows more hydrogen to diffuse into the melt surrounding the dendrites. The locally increased hydrogen concentration at the base of the dendrites achieves a partial pressure high enough for homogeneous pore formation. By adding an in-process laser powder drying step to the PBF-LB process for manufacturing of the parts the resulting hydrogen content of the parts could be reduced by up to 25%. This could decrease and even prevent the formation of hydrogen pores during laser welding. The reason for that is presumably the reduced partial pressure of hydrogen in the melt surrounding the dendrites during solidification. The laser drying process can be restricted to critical areas of the part and does not affect the resulting relative density of the manufactured part. It is thereby an excellent possibility to reduce hydrogen porosity when welding aluminum parts manufactured by PBF-LB.

As an outlook, the presented findings on the reduction of the hydrogen content could have an impact on the corrosion performance of PBF-LB manufactured parts. Corrosion performance of PBF-LB manufactured AlSi10Mg parts in the as built [44, 46] as well as in the heat-treated [62] condition and the role of hydrogen is a current research topic. Hydrogen embrittlement for example plays a crucial role during stress corrosion [45]. Further it is known that PBF-LB manufactured parts typically contain pores such as hydrogen pores, sometimes referred to as gas pores, or lack-of-fusion pores [63]. Hydrogen pores, due to their small size and round shape, do not significantly impact the mechanical performance of the parts [45, 64]. When put in environments with corrosive substances these pores can accelerate pit formation and pit growth and thereby drastically reduce the corrosion resistance [45]. It was proven by Weingarten et al. [39] that hydrogen porosity in PBF-LB manufactured parts can be reduced by in-process laser drying and the present study confirmed this also for laser welding of these parts. This could lead to a reduced susceptibility to corrosion and positively impact the corrosion performance. Moreover, hydrogen blistering during a subsequent heat treatment process could possibly be reduced by the additional process step. However, further research on these topics is needed to thoroughly assess the possible impacts of an in-situ laser powder drying process on the performance characteristics of PBF-LB manufactured AlSi10Mg parts.

Appendix

A1 Temporal sequence of the capillary shape.

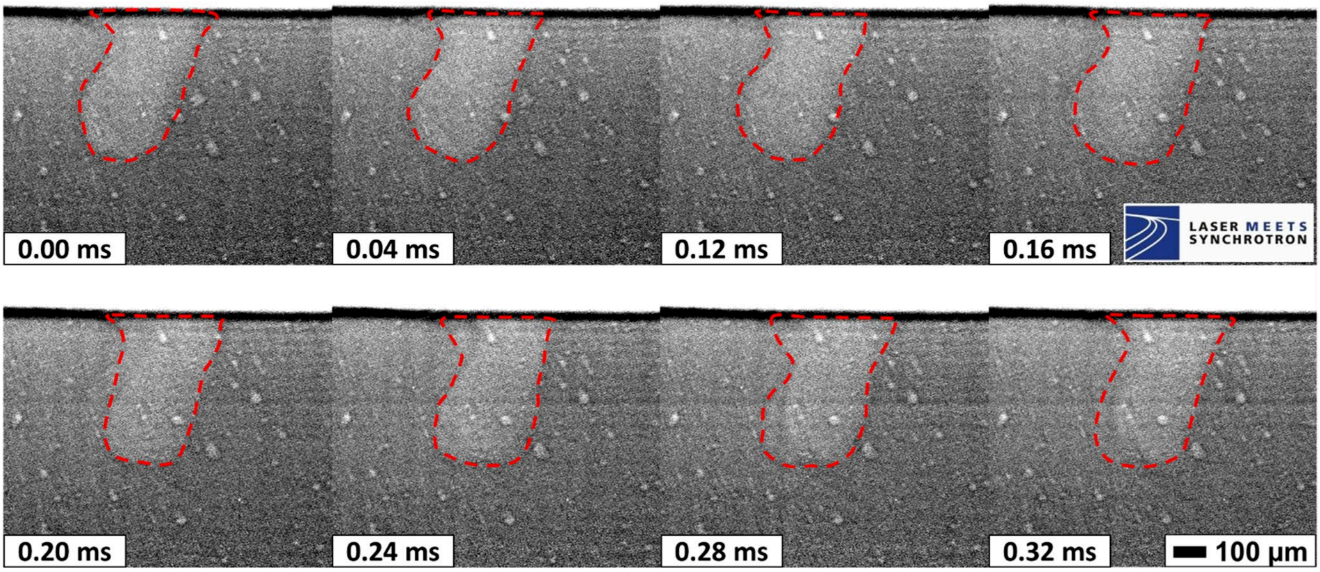

Fig. 13 Temporal sequence of the capillary shape with every second frame of the X-ray images. The capillary shows a stable U-shape and no collapses throughout the sequence

A2 X-ray image sequences:

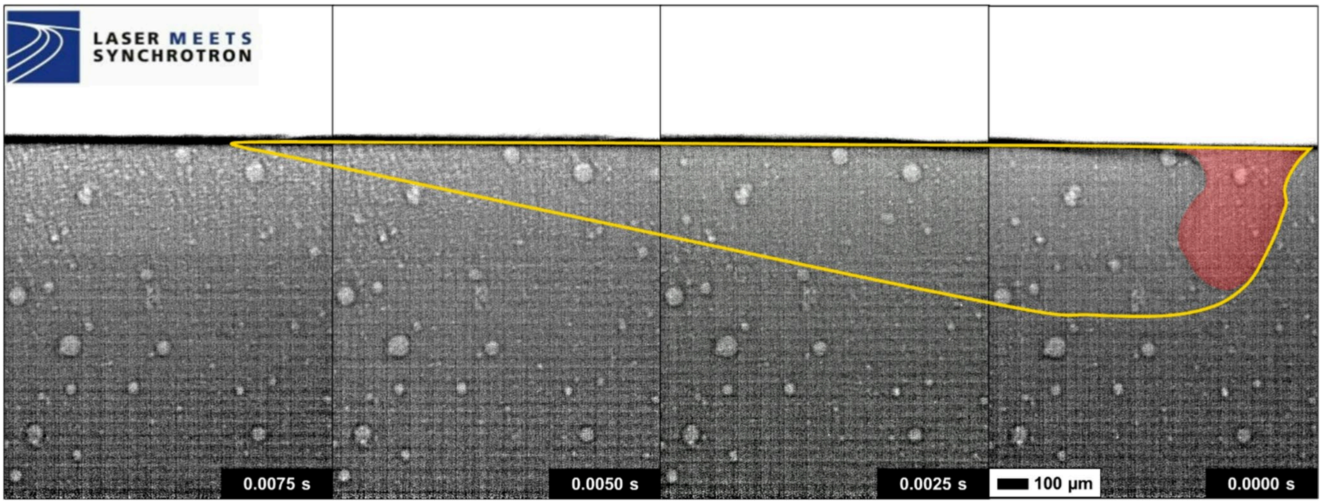

Fig. 14 X-ray image sequence D1 material

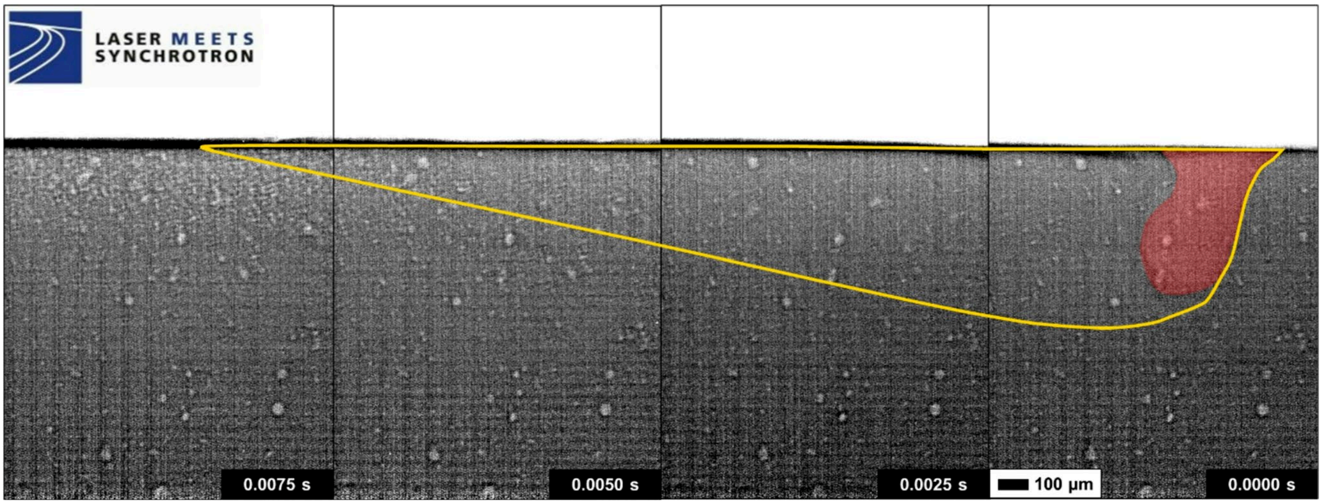

Fig. 15 X-ray image sequence D2 material

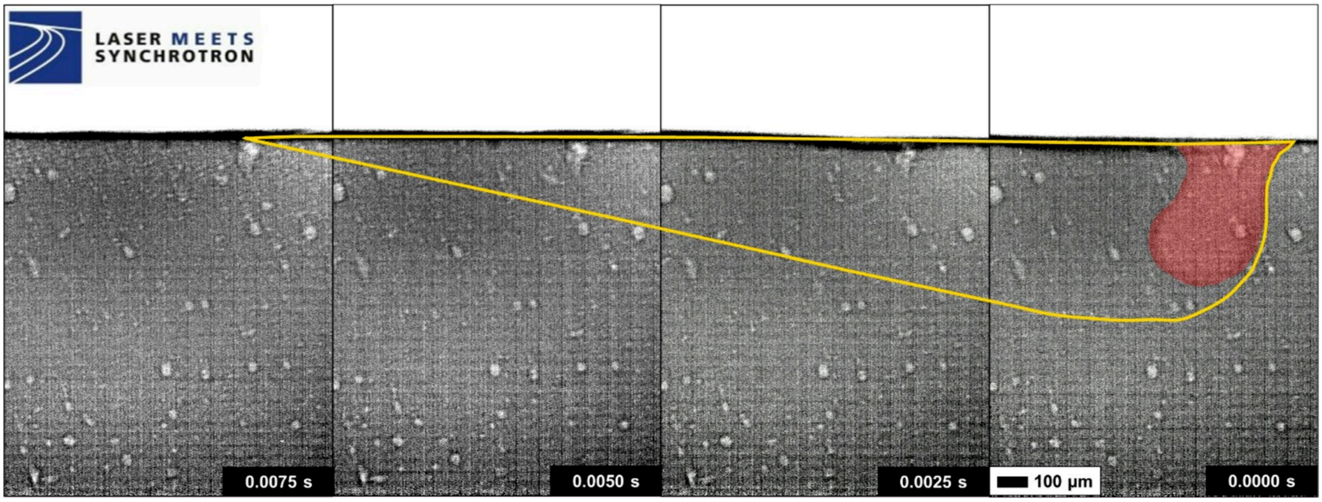

Fig. 16 X-ray image sequence D3 material

Supplementary Information The online version contains supplementary material available at https://doi.org/10.1007/s00170-025-17198-9.

Acknowledgements The authors would like to thank Dr.-Ing. Stefan Wagner (IAM – Karlsruhe Institute of Technology) for the fruitful discussions regarding hydrogen diffusion, Steffen Fritz (MPA – University of Stuttgart) for his support in calculating the solidification process and Petra Kalizan (ifm – University of Stuttgart) for her support in acquiring EDS analysis.

Author contributions Conceptualization: SK, VL, MJ, TG, VS & FZ; Methodology: SK & VL; Formal analysis: SK; Investigation: SK, VL, MH, JM, CS & GAF; Software: MH & JM; Data curation: SK; Visualization: SK; Resources: CS, AO, GAF & FZ; Funding Acquisition: CS, AO & MJ; Project administration: MJ; Supervision: MJ, TG & VS; Writing – original draft: SK; Writing – review & editing: VL, CS, MJ, TG, VS & FZ.

Funding Open Access funding enabled and organized by Projekt DEAL. The presented work was funded by the Ministry of Science, Research and the Arts of the Federal State of Baden-Wuerttemberg within the ‘InnovationCampus Future Mobility’, which is gratefully acknowledged. The presented investigations were carried out within the cooperation “Laser Meets Synchrotron” (www.laser-meets-synchrotron.de). The experimental setup and its operation were funded by the Deutsche Forschungsgemeinschaft e.V. (DFG, German Research Foundation) within the framework of the Collaborative Research Centre SFB1120-236616214 “Bauteilpräzision durch Beherrschung von Schmelze und Erstarrung in Produktionsprozessen”. The experiments were carried out in cooperation with Helmholtz-Zentrum Hereon in Hamburg at Beamline P61 of DESY PETRA III as part of proposal BAG-20230679 and we would like to thank G. Abreu Faria and all people involved for their support. The FIB-SEM FEI Helios NanoLab 600 was funded by the Deutsche Forschungsgemeinschaft (DFG, German Research Foundation) – 154585072.

Data availability The data presented in this study are available upon request to the corresponding author. All the data is presented within the article.

Declarations

Competing Interests The authors have no competing interests to declare that are relevant to the content of this article.

References

1. Liu X, Zhao C, Zhou X et al (2019) Microstructure of selective laser melted AlSi10Mg alloy. Mater Des 168:107677. https://doi.org/10.1016/j.matdes.2019.107677
2. Chen N, Wan Z, Wang H-P et al (2022) Effect of ambient pressure on laser welding of AlSi10Mg fabricated by selected laser melting. Mater Des 215:110427. https://doi.org/10.1016/j.matdes.2022.110427
3. Möller B, Schnabel K, Wagener R et al (2020) Fatigue assessment of additively manufactured AlSi10Mg laser beam welded to rolled EN AW-6082-T6 sheet metal. Int J Fatigue 140:105805. https://doi.org/10.1016/j.ijfatigue.2020.105805
4. Cui L, Peng Z, Chang Y et al (2022) Porosity, microstructure and mechanical property of welded joints produced by different laser welding processes in selective laser melting AlSi10Mg alloys. Opt Laser Technol 150:107952. https://doi.org/10.1016/j.optlastec.2022.107952

5. Mäkikangas J, Rautio T, Mustakangas A et al (2019) Laser welding of AlSi10Mg aluminium-based alloy produced by Selective Laser Melting (SLM). Procedia Manuf 36:88–94. https://doi.org/10.1016/j.promfg.2019.08.013
6. Zhang C, Bao Y, Zhu H et al (2019) A comparison between laser and TIG welding of selective laser melted AlSi10Mg. Opt Laser Technol 120:105696. https://doi.org/10.1016/j.optlastec.2019.105696
7. Gill M, Terry E, Abdi Y et al (2020) Joining technologies for metal additive manufacturing in the energy industry. JOM 72:4214–4220. https://doi.org/10.1007/s11837-020-04441-9
8. Biffi CA, Fiocchi J, Tuissi A (2019) Laser weldability of AlSi10Mg alloy produced by selective laser melting: microstructure and mechanical behavior. J Mater Eng Perform 28:6714–6719. https://doi.org/10.1007/s11665-019-04402-7
9. Heider A, Alter L (2024) Evaluation of pore formation during welding of copper using different laser sources. Procedia CIRP 124:383–387. https://doi.org/10.1016/j.procir.2024.08.138
10. Berger P, Hügel H, Graf T (2011) Understanding pore formation in laser beam welding. Phys Procedia 12:241–247. https://doi.org/10.1016/j.phpro.2011.03.031
11. Matsunawa A, Mizutani M, Katayama S et al (2003) Porosity formation mechanism and its prevention in laser welding. Weld Int 17:431–437. https://doi.org/10.1533/wint.2003.3138
12. Seto N, Katayama S, Matsunawa A (2001) Porosity formation mechanism and suppression procedure in laser welding of aluminium alloys. Weld Int 15:191–202. https://doi.org/10.1080/09507110109549341
13. Ardika RD, Triyono T, Muhayat N et al (2021) A review porosity in aluminum welding. Procedia Struct Integr 33:171–180. https://doi.org/10.1016/j.prostr.2021.10.021
14. Cross CE, Olson DL, Liu S (2003) Aluminum Welding. In: Totten GE, MacKenzie DS (eds) Handbook of Aluminum: Volume 7 Physical Metallurgy and Processes. Crc Press Inc., Bosa Roca, pp 481–532
15. Coniglio N, Cross CE (2009) Mechanisms for solidification crack initiation and growth in aluminum welding. Metall Mater Trans A 40:2718–2728. https://doi.org/10.1007/s11661-009-9964-4
16. Verhaeghe G, Hilton P, Barnes S (2003) Achieving low-porosity laser welds in aerospace aluminium alloy. SAE Trans 112:286–294
17. Miyagi M, Kawahito Y, Kawakami H et al (2017) Dynamics of solid-liquid interface and porosity formation determined through x-ray phase-contrast in laser welding of pure Al. J Mater Process Technol 250:9–15. https://doi.org/10.1016/j.jmatprotec.2017.06.033
18. Kutsuna M, Yan Q (1999) Study on porosity formation in laser welds of aluminium alloys (Report 2). mechanism of porosity formation by hydrogen and magnetism. Weld Int 13:597–611. https://doi.org/10.1080/09507119909447420
19. Gou G, Zhang M, Chen H et al (2015) Effect of humidity on porosity, microstructure, and fatigue strength of A7N01S-T5 aluminum alloy welded joints in high-speed trains. Mater Des 85:309–317. https://doi.org/10.1016/j.matdes.2015.06.177
20. Minhas N, Sharma V, Bhadauria SS (2023) A review on weldability and corrosion behaviour of L-PBF printed AlSi10Mg alloy. Can Metall Q 62:262–294. https://doi.org/10.1080/00084433.2022.2111968
21. Sun T, Ferguson N, Liu C et al (2022) Application of adjustable ring mode laser in remote laser welding of additive manufactured AlSi10Mg alloy. J Laser Appl. https://doi.org/10.2351/7.0000794
22. Wang C, He D, Cui L et al (2023) Influence of surface pretreatment on porosity and microstructure of laser welding in AlSi10Mg alloys sheets fabricated by laser powder bed fusion. Weld World 67:2449–2462. https://doi.org/10.1007/s40194-023-01579-3
23. Tiryakioğlu M (2020) The effect of hydrogen on pore formation in aluminum alloy castings: myth versus reality. Metals 10:368. https://doi.org/10.3390/met10030368
24. Yousefian P, Tiryakioğlu M (2018) Pore formation during solidification of aluminum: reconciliation of experimental observations, modeling assumptions, and classical nucleation theory. Metall Mater Trans A 49:563–575. https://doi.org/10.1007/s11661-017-4438-6
25. Talbot D (2004) Effects of Hydrogen in Aluminium and Its Alloys. Maney Publishing, Leeds
26. Kubo K, Pehlke RD (1985) Mathematical modeling of porosity formation in solidification. Metall Trans B 16:359–366
27. Lee PD, Hunt JD (2001) Hydrogen porosity in directionally solidified aluminum-copper alloys: a mathematical model. Acta Mater 49:1383–1398
28. Pequet C, Gremaud M, Rappaz M (2002) Modeling of microporosity, macroporosity, and pipe-shrinkage formation during the solidification of alloys using a mushy-zone refinement method: applications to aluminum alloys. Metall Mater Trans A 33:2095–2106
29. Atwood RC, Lee PD (2002) A three-phase model of hydrogen pore formation during the equiaxed dendritic solidification of Aluminum-Silicon alloys. Metall Mater Trans B 33:209–221
30. Campbell J (1968) The tribonucleation of bubbles. J Phys D Appl Phys 1:1085–1088
31. Yamamoto T, Komarov SV (2019) Development of a numerical model for hydrogen bubble generation, dynamics and trapping during solidification of aluminium alloys through Eulerian-Lagrangian framework. Int J Cast Met Res 32:266–277. https://doi.org/10.1080/13640461.2019.1690417
32. Campbell J (2006) An overview of the effects of bifilms on the structure and properties of cast alloys. Metall Mater Trans B 37:857–863
33. Dispinar D, Campbell J (2011) Porosity, hydrogen and bifilm content in al alloy castings. Mater Sci Eng A 528:3860–3865. https://doi.org/10.1016/j.msea.2011.01.084
34. El-Sayed MA, Griffiths WD (2014) Hydrogen, bifilms and mechanical properties of al castings. Int J Cast Met Res 27:282–287. https://doi.org/10.1179/1743133614Y.0000000113
35. Cao X, Campbell J (2005) Oxide inclusion defects in Al-Si-Mg cast alloys. Can Metall Q 44:435–448. https://doi.org/10.1179/cmq.2005.44.4.435
36. Trometer N, Chen B, Moodispaw M et al (2024) Modeling and validation of hydrogen porosity formation in aluminum laser welding. J Manuf Process 124:877–890. https://doi.org/10.1016/j.jmapro.2024.06.052
37. Gu C, Wei Y, Yu F et al (2017) Cellular automaton study of hydrogen porosity evolution coupled with dendrite growth during solidification in the molten pool of Al-Cu alloys. Metall Mater Trans A 48:4314–4323. https://doi.org/10.1007/s11661-017-4190-y
38. Weiss C, Heslenfeld J, Saewe JK et al (2022) Investigation on the influence of powder humidity in laser powder bed fusion (LPBF). Procedia CIRP 111:115–120. https://doi.org/10.1016/j.procir.2022.08.102
39. Weingarten C, Buchbinder D, Pirch N et al (2015) Formation and reduction of hydrogen porosity during selective laser melting of AlSi10Mg. J Mater Process Technol 221:112–120. https://doi.org/10.1016/j.jmatprotec.2015.02.013
40. Fiegl T, Franke M, Körner C (2022) Correlation of powder degradation, energy absorption and gas pore formation in laser-based powder bed fusion process of AlSi10Mg0.4. Addit Manuf 56:102917. https://doi.org/10.1016/j.addma.2022.102917
41. Strumza E, Hayun S, Barzilai S et al (2019) In situ detection of thermally induced porosity in additively manufactured and

sintered objects. J Mater Sci 54:8665–8674. https://doi.org/10.1007/s10853-019-03452-5

42. Gheysen J, Kashiwar A, Idrissi H et al (2023) Suppressing hydrogen blistering in a magnesium-rich healable laser powder bed fusion aluminum alloy analyzed by in-situ high resolution techniques. Materials & Design 231:112024. https://doi.org/10.1016/j.matdes.2023.112024
43. Yaokawa J, Oh-ishi K, Dong S et al (2023) Dimensional changes of selectively laser-melted AlSi10Mg alloy induced by heat treatment. Mater Trans 64:697–706. https://doi.org/10.2320/matertrans.MT-M2022165
44. Linder C, Vucko F, Ma T et al (2023) Corrosion-fatigue performance of 3D-printed (L-PBF) AlSi10Mg. Materials (Basel). https://doi.org/10.3390/ma16175964
45. Laieghi H, Kvvssn V, Butt MM et al (2024) Corrosion in laser powder bed fusion AlSi10Mg alloy. Eng Rep. https://doi.org/10.1002/eng2.12984
46. Gatto A, Cappelletti C, Defanti S et al (2023) The corrosion behaviour of additively manufactured alSi10Mg parts compared to traditional al alloys. Metals 13:913. https://doi.org/10.3390/met13050913
47. van Cauwenbergh P, Krishna MG, Bigot P, Thijs L et al (2019) Reducing Hydrogen Pores and Blisters by Novel Strategies and Tailored Heat Treatments for Laser Powder Bed Fusion of AlSi7Mg0.6. Proceedings Euro PM 2019
48. Lubkowitz V, Fayner L, Kramer S et al (2024) Comparison of in-process laser drying with furnace and vacuum drying to reduce moisture of AlSi10Mg powder processed in laser powder bed fusion. Procedia CIRP 124:135–140. https://doi.org/10.1016/j.procir.2024.08.086
49. Yamada T, Shobu T, Nishimura A et al (2012) In-situ X-Ray observation of molten pool depth during laser micro welding. J Laser Micro/Nanoeng 7:244–248
50. Schmidt L, Azizy R, Schricker K et al (2024) Describing the effect of local gas flow on keyhole and melt flow dynamics utilizing high-speed synchrotron X-ray imaging and numerical simulation. Procedia CIRP 124:553–558. https://doi.org/10.1016/j.procir.2024.08.173
51. Zhao C, Parab ND, Li X et al (2020) Critical instability at moving keyhole tip generates porosity in laser melting. Science. https://doi.org/10.1126/science.abd1587
52. Simonds BJ, Tanner J, Artusio-Glimpse A et al (2021) The causal relationship between melt pool geometry and energy absorption measured in real time during laser-based manufacturing. Appl Mater Today 23:101049. https://doi.org/10.1016/j.apmt.2021.101049
53. Lu W, Zhao L, Su Z et al (2025) Recent progress on in-situ characterization of laser additive manufacturing process by synchrotron radiation. J Mater Sci Technol 217:29–46. https://doi.org/10.1016/j.jmst.2024.07.047
54. Reinheimer EN, Berger P, Hagenlocher C et al (2024) Supercritical melt flow in high-speed laser welding and its interdependence with the geometry of the keyhole and the melt pool. Int J Adv Manuf Technol 131:4253–4266. https://doi.org/10.1007/s00170-024-13266-8
55. Tang M, Pistorius PC, Narra S et al (2016) Rapid solidification: selective laser melting of AlSi10Mg. JOM 68:960–966. https://doi.org/10.1007/s11837-015-1763-3
56. Anyalebechi PN (2022) Hydrogen solubility in liquid and solid pure Aluminum—critical review of measurement methodologies and reported values. MSA 13:158–212. https://doi.org/10.4236/msa.2022.134011
57. Anyalebechi PN (1995) Analysis of the effects of alloying on the hydrogen solubility in liquid aluminum alloys. Scr Metall Mater 33:1209–1216
58. Scheil E (1942) Bemerkungen Zur schichtkristallbildung. Int J Mater Res 34:70–72. https://doi.org/10.1515/ijmr-1942-340303
59. Kou S (2003) Welding metallurgy, 2nd edn. Wiley-Interscience, Hoboken N.J
60. Hegde S, Prabhu KN (2008) Modification of eutectic silicon in Al–Si alloys. J Mater Sci 43:3009–3027. https://doi.org/10.1007/s10853-008-2505-5
61. Anyalebechi PN (2016) Analysis and thermodynamic prediction of hydrogen solution in solid and liquid multicomponent aluminum alloys. In: Grandfield JF, Eskin DG (eds) Essential readings in light metals. Springer International Publishing, Cham, pp 185–200
62. Islam T, Zhao B, Ghinatti E et al (2026) Linking printing layer thickness to performance-critical microstructure and corrosion in LPBF AlSi7Mg. Mater Chem Phys 347:131395. https://doi.org/10.1016/j.matchemphys.2025.131395
63. Hastie JC, Kartal ME, Carter LN et al (2020) Classifying shape of internal pores within AlSi10Mg alloy manufactured by laser powder bed fusion using 3D X-ray micro computed tomography: influence of processing parameters and heat treatment. Mater Charact 163:110225. https://doi.org/10.1016/j.matchar.2020.110225
64. Gong H, Rafi K, Gu H et al (2015) Influence of defects on mechanical properties of Ti–6Al–4V components produced by selective laser melting and electron beam melting. Mater Des 86:545–554. https://doi.org/10.1016/j.matdes.2015.07.147